

ARTICLE

Received 23 Jan 2017 | Accepted 23 Feb 2017 | Published 21 Apr 2017

DOI: 10.1038/ncomms15113

OPEN

# Electrochemical generation of sulfur vacancies in the basal plane of MoS<sub>2</sub> for hydrogen evolution

Charlie Tsai<sup>1,2,\*</sup>, Hong Li<sup>3,4,\*</sup>, Sangwook Park<sup>3,\*</sup>, Joonsuk Park<sup>5</sup>, Hyun Soo Han<sup>3</sup>, Jens K. Nørskov<sup>1,2</sup>, Xiaolin Zheng<sup>3</sup> & Frank Abild-Pedersen<sup>1,2</sup>

Recently, sulfur (S)-vacancies created on the basal plane of 2H-molybdenum disulfide (MoS<sub>2</sub>) using argon plasma exposure exhibited higher intrinsic activity for the electrochemical hydrogen evolution reaction than the edge sites and metallic 1T-phase of MoS<sub>2</sub> catalysts. However, a more industrially viable alternative to the argon plasma desulfurization process is needed. In this work, we introduce a scalable route towards generating S-vacancies on the MoS<sub>2</sub> basal plane using electrochemical desulfurization. Even though sulfur atoms on the basal plane are known to be stable and inert, we find that they can be electrochemically reduced under accessible applied potentials. This can be done on various 2H-MoS<sub>2</sub> nanostructures. By changing the applied desulfurization potential, the extent of desulfurization and the resulting activity can be varied. The resulting active sites are stable under extended desulfurization durations and show consistent HER activity.

<sup>1</sup>SUNCAT Center for Interface Science and Catalysis, Department of Chemical Engineering, Stanford University, 443 Via Ortega, Stanford, California 94305, USA. <sup>2</sup>SUNCAT Center for Interface Science and Catalysis, SLAC National Accelerator Laboratory, 2575 Sand Hill Road, Menlo Park, California 94305, USA. <sup>3</sup>Department of Mechanical Engineering, Stanford University, 440 Escondido Mall, Stanford, California 94305, USA. <sup>4</sup>School of Mechanical and Aerospace Engineering, Nanyang Technological University, Singapore 639798, Singapore. <sup>5</sup>Department of Material Science & Engineering, Stanford University, 440 Escondido Mall, Stanford, California 94305, USA. \* These authors contributed equally to this work. Correspondence and requests for materials should be addressed to X.Z. (email: xlzheng@stanford.edu) or to F.A.-P. (email: abild@slac.stanford.edu).

Molybdenum disulfide ( $\text{MoS}_2$ )-based catalysts for the electrochemical (EC) hydrogen evolution reaction (HER) have attracted intensified research in recent years due to their earth abundance and potential to become highly active alternatives to platinum catalysts. Ever since the edge sites of  $2H$ - $\text{MoS}_2$  were theoretically predicted<sup>1</sup> and experimentally verified<sup>2,3</sup> to be the active sites for hydrogen evolution, subsequent efforts have largely focused on maximally exposing such edge sites through nano-structuring techniques<sup>3–5</sup>. The basal plane, which usually constitutes the bulk of the material, has only recently been considered as a possible source of active sites, with the  $1T$ -phase<sup>6–8</sup> being one of the first examples. Very recently, we demonstrated that active sites could be directly created on the basal plane of common  $2H$ - $\text{MoS}_2$  materials by generating sulfur (S)-vacancies, whose intrinsic activity can be optimized by fine tuning the S-vacancy concentration and introducing elastic tensile strain<sup>9</sup>. At the S-vacancy sites, the under-coordinated Mo atoms introduce gap states that allow for favourable hydrogen binding, leading to the highest per-site turnover frequency (TOF) reported for any  $\text{MoS}_2$ -based catalyst for HER. Though  $\text{MoS}_2$  catalysts are increasingly being considered for various electro-catalytic processes, the potential roles of these newly discovered S-vacancy sites are still unknown. In addition, the S-vacancies in the basal plane have so far only been generated using controlled argon (Ar) plasma exposure and  $\text{H}_2$  annealing<sup>10</sup>. This approach is only effective for flat  $\text{MoS}_2$  catalysts due to the Ar plasma's directionality and is thus unsuitable for large-scale synthesis<sup>11</sup>. As such, the possibility of creating S-vacancies in other  $\text{MoS}_2$ -based materials has not yet been demonstrated. To fully utilize S-vacancies in  $\text{MoS}_2$  catalysts for industrial applications, a facile, general and scalable route for generating S-vacancies in  $\text{MoS}_2$  of any morphology is needed.

One possibility for generating S-vacancies is to remove sulfur atoms from the basal plane electrochemically. This idea involves reducing the sulfur atoms in the basal plane of  $2H$ - $\text{MoS}_2$  to form hydrogen sulfide ( $\text{H}_2\text{S}$ ) gas via a desulfurizing 'activation' cycle, similar to the oxygen vacancies generated in metal oxides under applied cathodic potentials<sup>12</sup>.

Herein, we present an EC process for generating S-vacancies in monolayer as well as polycrystalline multilayer  $\text{MoS}_2$  supported on various electrodes. We use density functional theory (DFT) calculations to show that the formation of S-vacancies in the basal plane is expected to be thermodynamically favourable at a sufficiently reducing potential. Sulfur atoms in the basal plane are hydrogenated and then removed as  $\text{H}_2\text{S}$  gas to form the S-vacancies. The concentration of S-vacancies can be varied by changing the applied desulfurization voltage. These predictions are experimentally verified on a well-defined model system of continuous  $\text{MoS}_2$  monolayers supported on gold (Au) (the same system considered previously<sup>9</sup>), thus showing that electrochemically generated S-vacancies are comparable to Ar plasma generated ones. We further demonstrate the generality of the EC approach by electrochemically generating S-vacancies on multilayered  $\text{MoS}_2$  supported on flat carbon rods and porous carbon foam, leading to significantly improved HER activity in both cases. Finally, using  $\text{MoS}_2$  supported on carbon foam, we show that the HER activity is stable under extended desulfurization durations as well as operating durations and that the concentration of S-vacancies and activity can be varied using the applied potential.

## Results

**Theoretical predictions.** Using DFT calculations, we investigated the conditions where S-vacancies in the  $2H$ - $\text{MoS}_2$  basal planes become thermodynamically favoured in an EC environment. Using a descriptor-based analysis with the hydrogen adsorption free energy<sup>9</sup>, we showed previously that edge vacancies are not expected to increase HER activity. Hence, we focus on the basal plane in this work. The surface free energies per unit cell (relative to pristine  $\text{MoS}_2$ ) as a function of the applied potential were determined for pristine  $\text{MoS}_2$ ,  $\text{MoS}_2$  with S-vacancies (3.1% surface vacancies) and  $\text{MoS}_2$  with various species adsorbed on the S-vacancy (Fig. 1a). The exact values of the surface energies depend on a reference pressure of  $\text{H}_2\text{S}$  gas, which we have chosen as  $10^{-8}$  bar according to standard corrosion

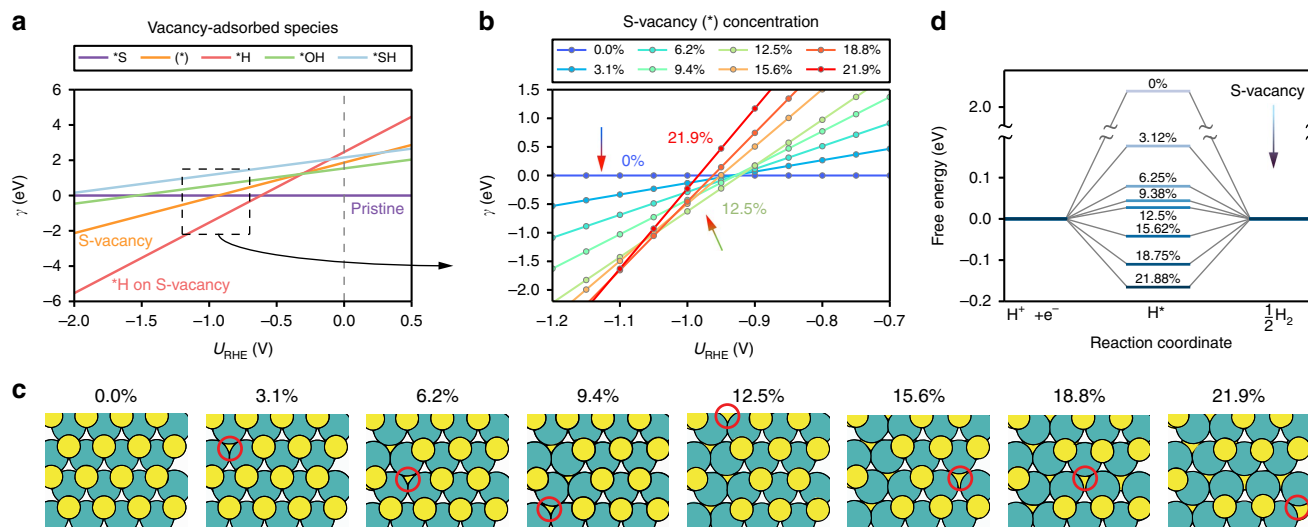


**Figure 1 | Theoretical predictions.** (a) Surface energy per unit cell for  $2H$ - $\text{MoS}_2$  as a function of applied potential for the basal plane of  $2H$ - $\text{MoS}_2$  with different adsorbate species at a fixed sulfur vacancy (3.1%). The surface energies of various species in the S-vacancy are shown. (\*) Refers to a S-vacancy and the adsorbed species in the S-vacancy are denoted by \*prefix. \*S refers to sulfur adsorbed in the vacancy, that is, a pristine basal plane without S-vacancies. (b) Surface energy per unit cell for a range of S-vacancy concentrations, without any adsorbates. The concentration of S-vacancies varies from 0 to 21.9% within the narrow range of  $-1.0$  V to  $-1.1$  V. In all cases, the surface energies are taken relative to a pristine basal plane ( $\gamma = 0$  eV). (c) When the S-vacancy sites are generated in succession, S-vacancies are most stable when formed next to an existing S-vacancy. (d) Free energy diagram for the HER on S-vacancy sites. The results represent hydrogen adsorption on the most stable site within the computational cell.

resistance<sup>13</sup>. Although the energies of all surfaces involving a vacancy will be lower if a smaller pressure is chosen, the qualitative trends and relative energies between the different surfaces are independent of the reference.

At around  $-1.0$  V versus RHE, the surface with S-vacancies (\*) becomes stable compared to the pristine basal plane (\*S). Hydrogen adsorption onto the S-vacancy site (\*H) becomes more thermodynamically favoured compared to either the re-adsorption of sulfur (\*S) below  $-0.3$  V versus RHE (Fig. 1a) or \*OH poisoning. This indicates that generated S-vacancies will be immediately occupied by hydrogen and that the removed  $\text{H}_2\text{S}$  gas is unlikely to return. Hence, only H atoms are expected to adsorb in the generated S-vacancies throughout the desulfurization process and even after the applied potential is turned off. It should then be possible to permanently activate the  $\text{MoS}_2$  basal plane in a desulfurizing step.

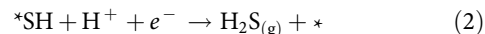
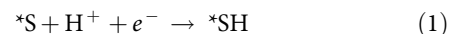
We further compare the surface energies per unit cell (relative to pristine  $\text{MoS}_2$ ) of an empty S-vacancy as a function of the applied potential for a wide range of S-vacancy (\*) coverages (Fig. 1b shows a zoomed-in region of the applied potential). Larger amounts of vacancies are stabilized at more negative potentials, indicating that the applied potential can be used to vary the concentration of S-vacancies. The formation of 3.1% S-vacancies on the surface ( $\gamma \leq 0$  eV) occurs around  $-1.0$  V versus RHE, which is similar to the surface energies for both 6.2 and 9.4% S-vacancies but higher than that of 12.5% S-vacancies. This is because vacancies tend to form in clusters to stabilize the system (Fig. 1c, see Supplementary Table 1, Supplementary Fig. 1, Supplementary Note 2 and a transmission electron microscopy (TEM) image in Supplementary Fig. 2 and Supplementary Note 3 for further details of this behaviour), and clustered vacancies have lower energies than evenly dispersed ones. Once the first S-vacancy is formed, successive S-vacancies are more readily made in their vicinity. They first follow a zigzag pattern and then branch out once a continuous repeating zigzag (within our computational cell) is formed. The lowest energy of 12.5% corresponds to a periodically repeating and continuous zigzag of S-vacancies in the computational cell. We note that there could be intermediate coverages of S-vacancies following the zigzag configuration that are not representable by the unit cell size in this study.

Beyond 12.5% vacancies, however, the energetic cost of forming a vacancy outweighs the stabilization from forming clusters of vacancies. Although it appears that either a 12.5, 15.6 or 21.9% coverage of S-vacancies will be most stable at potentials

lower than  $-1.0$  V versus RHE, many of them are similar in energy. There could also be additional kinetic barriers towards forming the S-vacancies that are not yet considered here. Regardless, the entire range of S-vacancy coverages considered herein becomes thermodynamically accessible below  $-1.0$  V versus RHE.

We showed recently that the optimal hydrogen adsorption free energy  $\Delta G_{\text{H}} = 0$  eV for HER occurs for an S-vacancy concentration that is between 12.5 and 15.62% of the surface atoms. Although our previous results were performed on  $\text{MoS}_2$  with evenly spread out S-vacancies, we find that the  $\Delta G_{\text{H}}$  and associated trends are nearly the same on  $\text{MoS}_2$  with clustered vacancies (Fig. 1d). The values of  $\Delta G_{\text{H}}$  are well within 0.1 eV of each other. The 12.5 and 15.62% concentrations are lowest in free energy at potentials from  $-0.97$  to  $-1.15$  V versus RHE (Fig. 1b). The values of  $\Delta G_{\text{H}}$  for all other S-vacancy concentrations are also within  $\pm 0.1$  eV and correspond to highly active sites for HER.

The surface energies only reflect the overall thermodynamic process and do not take into account the intermediate steps, which could have larger energetic requirements. However, it is useful for comparing the relative stabilities of the different desulfurization extents. To verify whether the surface energies adequately reflect the trends, the full reaction pathway needs to be determined as well. The desulfurization process is expected to occur via the proton and electron transfer to the sulfur atoms in the basal plane:  $*\text{S} + 2(\text{H}^+ + \text{e}^-) \rightarrow * + \text{H}_2\text{S}_{(\text{g})}$ , where the hydrogenated sulfur atom (\*SH) is removed as  $\text{H}_2\text{S}$  gas, leaving behind a S-vacancy (\*) (Fig. 2a). Here \* denotes a S-vacancy and the \* prefix indicates a species adsorbed on the S-vacancy. The pristine basal plane is thus referred to as \*S. This process can occur through the two proton–electron transfer steps as follows:



Using the computational hydrogen electrode, the chemical potential of the proton–electron pair can be calculated relative to that of hydrogen gas, allowing for the potential-dependent free energy to be determined<sup>14,15</sup> (see Methods section). The reaction steps are shown in the free energy diagram and the schematic in Fig. 2a. At 0 V versus RHE, the first protonation to form \*SH (equation 1) is uphill by 1.24 eV and hydrogen adsorbs extremely weakly, in agreement with the observation that the pristine basal plane of  $\text{MoS}_2$  is inert towards hydrogen evolution at moderate

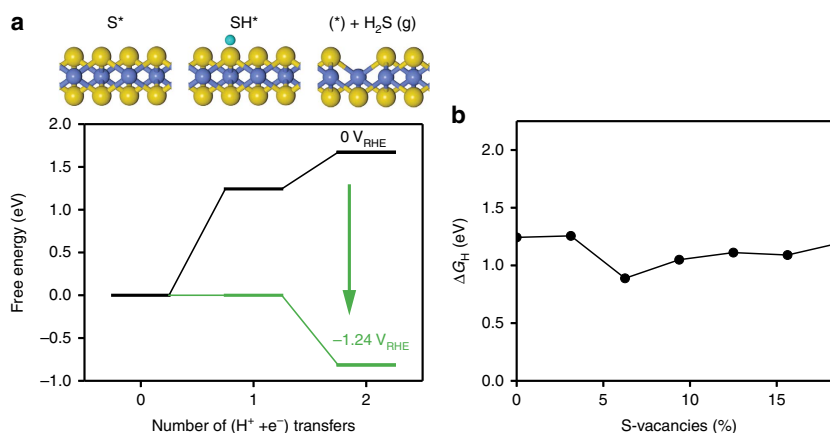


**Figure 2 | The EC desulfurization process.** (a) Free energy diagram for the protonation and removal of S. The green line indicates the free energy pathway at the applied potential required to make all paths exergonic. An illustration of the EC desulfurization process corresponding to the steps is shown above the plot. (b) Hydrogen adsorption free energy ( $\Delta G_{\text{H}}$ ) onto a sulfur atom on the basal plane for each concentration of S-vacancies.

potentials (solvation effects have been included in the calculations using one layer of explicit charged solvent<sup>16</sup>, where  $\Delta G_{\text{H}}$  was found  $-0.65$  eV lower compared to previous calculations in vacuum<sup>17,18</sup>). Adsorption of the second proton to form gaseous  $\text{H}_2\text{S}$  (equation 2) is  $0.42$  eV uphill from the first step. Nevertheless, both steps become exergonic at a potential of  $-1.24$  V versus RHE. This is a  $\sim 0.24$  V higher cathodic potential than the required potential determined by the equilibrium surface energy diagrams (Fig. 1b), indicating that the desulfurization reaction needs to overcome an additional  $0.24$  eV compared to the results from the surface energy diagrams. However, the  $\Delta G_{\text{H}}$  required for reaction step in equation (1) is approximately the same for all S-vacancy concentrations studied herein (Fig. 2b), which indicates that the surface free energies of the S-vacancies (Fig. 1b) will determine which S-vacancy concentration is most stable. The results in Fig. 1 should thus sufficiently describe those trends qualitatively.

**Experimental verification.** To experimentally verify our theoretical predictions, we tested the EC process for generating S-vacancies in monolayer and multilayer  $\text{MoS}_2$  catalysts supported on various electrodes. We first synthesized continuous  $2\text{H-MoS}_2$  monolayers with large single-crystal domains ( $> 100 \mu\text{m}$ ) supported on a Au substrate (see Method section for details). This well-defined model system maximizes the exposure of basal plane sites and minimizes the presence of edge sites, which enables us to unambiguously identify the effects of the desulfurization process on the HER activity of the basal planes of  $2\text{H-MoS}_2$ . This also allows us to draw direct comparisons with our recent work, where S-vacancies were generated using Ar plasma treatment on the exact same model system. Since S-vacancies are expected to become stable starting at  $-1.0$  V versus RHE (Fig. 1a,b), the desulfurization process was performed by decreasing the potential to  $-1.0$  V versus RHE using linear sweep voltammetry (LSV) with a sweeping speed of  $50 \text{ mV s}^{-1}$ . After the desulfurization process, the desulfurized sample with vacancies (V- $\text{MoS}_2$ , Fig. 3a) shows observable morphological change (scanning electron microscopy (SEM) image) compared to the pristine as-synthesized catalyst (P- $\text{MoS}_2$ , Fig. 3a) suggesting the formation of defects.

To further confirm the selective removal of S atoms by the EC desulfurization process, we compared the S:Mo atomic ratio between P- $\text{MoS}_2$  and V- $\text{MoS}_2$  using X-ray photoelectron spectroscopy (XPS). The Mo 3d peaks (Fig. 3b) are similar for P- $\text{MoS}_2$  and V- $\text{MoS}_2$ , suggesting that the Mo atoms are not significantly affected. However, the S 2p peaks for V- $\text{MoS}_2$  are much weaker than those of P- $\text{MoS}_2$  (Fig. 3c), confirming the removal of S atoms during the desulfurization process. For these particular XPS spectra, the S:Mo peak area ratio for V- $\text{MoS}_2$  is about 25% smaller than of P- $\text{MoS}_2$ , corresponding to  $\sim 25\%$  S-vacancies. We used the major peaks (marked as shaded areas in Fig. 3b,c) to calculate the atomic ratio of S:Mo while that of the as-grown  $\text{MoS}_2$  is normalized to 2.0. We note that the S-vacancy percentage was not spatially uniform across the sample surface, which could be due to the clustering of S-vacancies observed in the DFT results and TEM image (Supplementary Fig. 2).

We further compared the HER catalytic activity of V- $\text{MoS}_2$  (EC) with P- $\text{MoS}_2$ . As shown in Fig. 3d, the current density of V- $\text{MoS}_2$  (EC) is considerably higher than that of P- $\text{MoS}_2$ . Any activity from P- $\text{MoS}_2$  likely comes from the minority of exposed edge sites in the continuous monolayers or intrinsic defects in the catalyst, which would create edges or basal plane vacancies. To quantify the improvement, we define a normalized current density increment  $\Delta J/J_0$ , where  $J_0$  is the current density of P- $\text{MoS}_2$  and  $\Delta J$  is the current density increase at  $-0.32$  V versus RHE

(Fig. 3d). We tested six monolayer  $\text{MoS}_2$  samples with an average S-vacancy concentration about  $(15 \pm 8)\%$ , and their  $\Delta J/J_0$  values range  $(438 \pm 159)\%$ , confirming the generation of catalytically active S-vacancies using the EC process. We then calculated the TOF normalized to the number of surface Mo atoms ( $\text{TOF}_{\text{Mo}}$ ) to compare the intrinsic HER activities for the S-vacancy sites. As shown in Fig. 3e, the  $\text{TOF}_{\text{Mo}}$  for V- $\text{MoS}_2$  (EC) is more than an order of magnitude higher than that of P- $\text{MoS}_2$  in certain potential ranges. Importantly, the  $\text{TOF}_{\text{Mo}}$  for V- $\text{MoS}_2$  (EC) is comparable to the previously reported V- $\text{MoS}_2$  (Ar plasma treatment<sup>9</sup>) with the same range of S-vacancy concentrations (grey colour area in Fig. 3e). The quantitative comparison clearly shows that the EC desulfurization process is as effective as the Ar plasma treatment<sup>9</sup> for generating highly active S-vacancy sites. Finally, it should be noted that S-vacancies are not only active for HER but also improves the electron injection from the  $\text{MoS}_2$  to the substrate<sup>19</sup>. Both factors contribute to the observed high-intrinsic HER activity of the S-vacancy.

The EC desulfurization process should be a general procedure for generating S-vacancies on any  $\text{MoS}_2$  electrodes since it simply reduces S atoms on the surface. It thus acts as a post-synthesis activation procedure. To verify this, we applied the desulfurization process to various  $2\text{H-MoS}_2$  systems including polycrystalline  $2\text{H-MoS}_2$  grown on commercial carbon rods and foams<sup>20</sup> (Fig. 4a). The desulfurization process was performed by applying a constant voltage using chronoamperometry with a 60 s interval unless specified otherwise. These supported polycrystalline multilayer  $\text{MoS}_2$  materials differ from monolayer  $\text{MoS}_2$  (Fig. 3) in both surface area and electrode morphology. After the desulfurization process, the polycrystalline multilayer  $\text{MoS}_2$  supported on carbon foam appears the same through optical and SEM inspection (Fig. 4a), but their HER catalytic activity shows a pronounced improvement with a  $\Delta J/J_0$  of about three-fold (333%) (Fig. 4b). The activity enhancement caused by desulfurization is even more obvious if we compare the J-V curves after iR correction (dashed curves). Comparing the iR-corrected curve of P- $\text{MoS}_2$  (blue dashed curve) and V- $\text{MoS}_2$  (red dashed curve), there is an  $\sim 12$  times current density increment (at  $-0.32$  V versus RHE) due to the desulfurization (corresponding Tafel plot shown in Fig. 4c). The Tafel slopes are greatly decreased due to desulfurization in both cases for before (from 217 to 193  $\text{mV dec}^{-1}$ ) and after iR correction (151 to 102  $\text{mV dec}^{-1}$ ). These comparisons suggest that the HER kinetics of the desulfurized sample is much faster than that of the pristine sample<sup>21</sup>.

Having demonstrated the generality of the EC S-vacancy generation, we then investigated how the HER activity can be varied w.r.t. the desulfurization duration and the desulfurization voltage. For this study, we used the polycrystalline multilayer  $\text{MoS}_2$  supported on carbon foam because they are more durable than the  $\text{MoS}_2$  monolayers, and have better performance than those on carbon rods. An 8 h long stability test was performed, where the current was stable for the full duration (Supplementary Fig. 4 and Supplementary Note 5). As shown in Fig. 4d, the desulfurization process was carried out at different cathodic potentials. Under each potential, the desulfurization process was carried out in an interval up to 10 min. Overall, the HER activity of  $\text{MoS}_2$  multilayers improves with increasing desulfurization voltage. For each desulfurization voltage, the HER activity of  $\text{MoS}_2$  multilayers also first increases with increasing desulfurization duration and then levels off. This is likely due to the competition between the desulfurization reaction and HER. As more S-vacancies are generated, more sites could become available for HER, which inhibits further desulfurization and leads to a steady-state coverage of S-vacancies. There is thus minimal risk in fully desulfurizing the  $\text{MoS}_2$  into Mo metal.

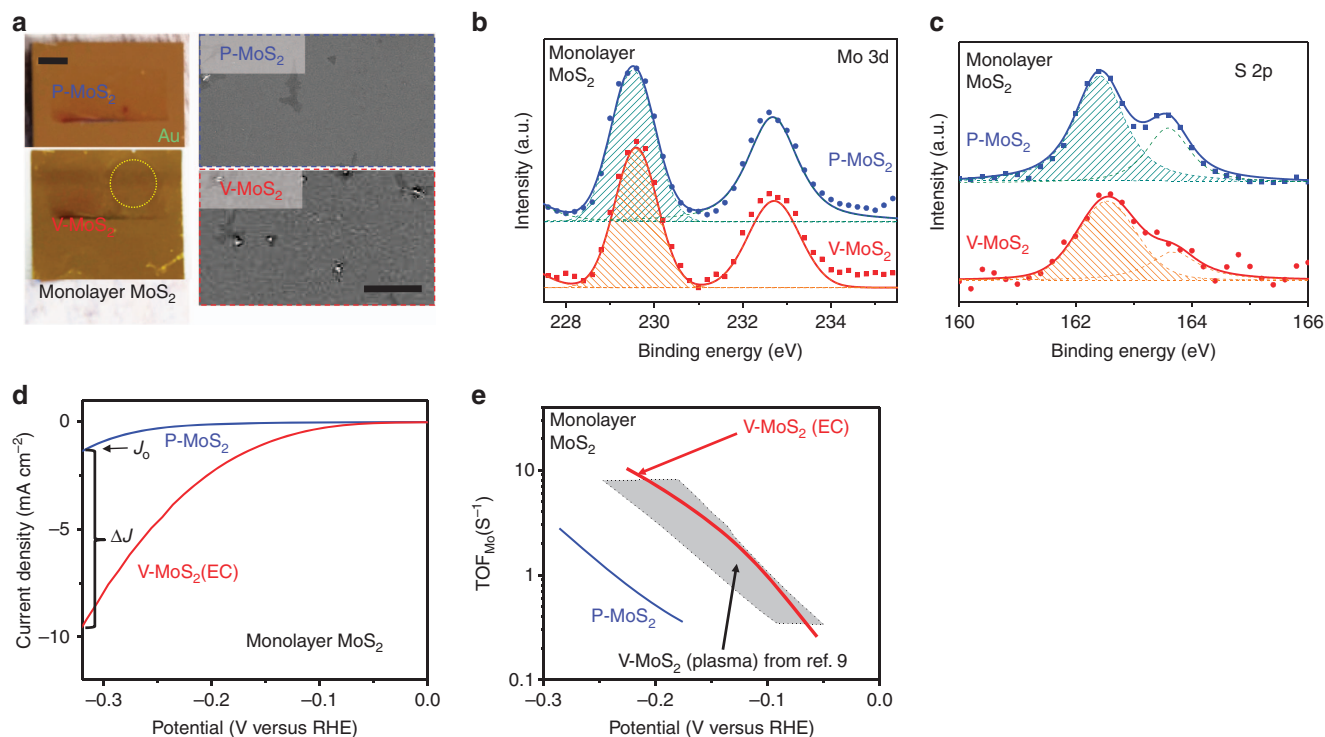


**Figure 3 | Characterizations and catalytic activity of monolayer MoS<sub>2</sub>.** (a) Optical (left panel; scale bar, 2 mm) and SEM images (right panel; scale bar, 20 μm) of monolayer MoS<sub>2</sub> film before (P-MoS<sub>2</sub>, upper panel) and after (V-MoS<sub>2</sub>, lower panel) desulfurization. (b) XPS Mo 3d and (c) S 2p peaks of pristine MoS<sub>2</sub> (P-MoS<sub>2</sub>, upper curves) and MoS<sub>2</sub> with S-vacancies (V-MoS<sub>2</sub>, lower curves). The filled symbols are measured data, and the solid lines are the parametric fits. The dashed lines with enclosed shaded areas label the major peak used to characterize the S:Mo atomic ratio. (d) LSV of monolayer MoS<sub>2</sub> before and after desulfurization. The current density increment is defined as  $\Delta J/J_0$ , where  $J_0$  is the current density at  $-0.32$  V versus RHE before desulfurization. (e) TOF per surface Mo atom ( $\text{TOF}_{\text{Mo}}$ ) as a function of applied potential for MoS<sub>2</sub> monolayers before and after desulfurization. The results from previous work where Ar plasma was employed for desulfurization are also shown for comparison (shaded area). All the current densities are defined based on the total electrode surface area.

We further plotted the steady-state  $\Delta J/J_0$  (desulfurization with 10 min interval in Fig. 4d) as a function of the applied desulfurization voltage (Fig. 4e, left y axis). The corresponding S:Mo atomic ratios for those conditions were measured using inductively coupled plasma optical emission spectroscopy (ICP-OES) (Fig. 4e, right y axis). First, the desulfurization process has an onset potential of about  $-0.6$  V versus RHE. According to our theoretical predictions (Fig. 1a), this is where hydrogen begins to adsorb onto existing vacancy sites. Second, the desulfurization is most effective between  $-0.6$  and  $-1.2$  V versus RHE as indicated by the sharp decrease of S:Mo atomic ratio and increase of  $\Delta J/J_0$ . In line with our predictions, this is the region where a vacancy-rich surface and a pristine surface are predicted to have comparable equilibrium surface energies (Fig. 1). Finally, the desulfurization effect levels off beyond  $-1.3$  V versus RHE. The levelling off of the current density increment is predicted by our theoretical calculation in that successive S-vacancies generation becomes increasingly difficult at higher S-vacancy concentrations (Fig. 1b). The desulfurization voltage and the desulfurization time are thus effective knobs for tuning the final activity of the vacancy-rich MoS<sub>2</sub> catalysts.

We also conducted a control experiment by applying the desulfurization process to the support only (without MoS<sub>2</sub>). Figure 5a summarizes the effect of the EC desulfurization process on all samples (See Supplementary Fig. 6 for detailed sample statistics). First, the support substrate (carbon rod, carbon foam and Au) did not show any observable current density enhancement (Fig. 5a, unfilled bars), indicating that the desulfurized MoS<sub>2</sub> catalyst is responsible for the enhanced HER activity. Second, the EC desulfurization process improves the HER activity

of MoS<sub>2</sub> monolayers the most, which is due to the predominance of basal plane sites in the continuous pristine monolayers and absence of Ohmic loss due to interlayer tunnelling<sup>22</sup>. Third, the enhancement effect is smaller for the MoS<sub>2</sub> multilayers supported on carbon. This is partly due to the polycrystalline nature of the multilayers (grain size  $<100$  nm), which will have a relatively higher ratio of edge sites to basal plane sites than that of a perfect monolayer. Hence, the edge sites contribute to the measured HER activity even after desulfurization. Even in this case, the desulfurization process can triple the current density, confirming a significant contribution from the activated basal plane sites.

**Comparisons to state-of-the-art catalysts.** It should be noted that the current density and Tafel slopes of the desulfurized MoS<sub>2</sub> are lower than some of the best MoS<sub>2</sub> electrodes reported in the literature<sup>6,7,23</sup>. This is partially because our current density was normalized to the total electrode area rather than the projected area, and the morphology of the MoS<sub>2</sub> catalysts have not yet been optimized in this work. The current densities and Tafel slopes are also greatly affected by the loading of the catalyst. It is important to plot the intrinsic activity, in term of TOF per surface Mo atom, to make a fair comparison between different catalysts and understand the effect of EC desulfurization independent of catalyst loading. Figure 5b shows the TOF per surface Mo atom ( $\text{TOF}_{\text{Mo}}$ ) versus applied potential of our samples, together with those MoS<sub>x</sub>-based HER electrocatalysts considered state of the art. The grey curves represent these MoS<sub>x</sub> electrocatalysts, including edge sites, amorphous cluster, nanowire, mesoporous film and so on, summarized in ref. 24. The upper right light-

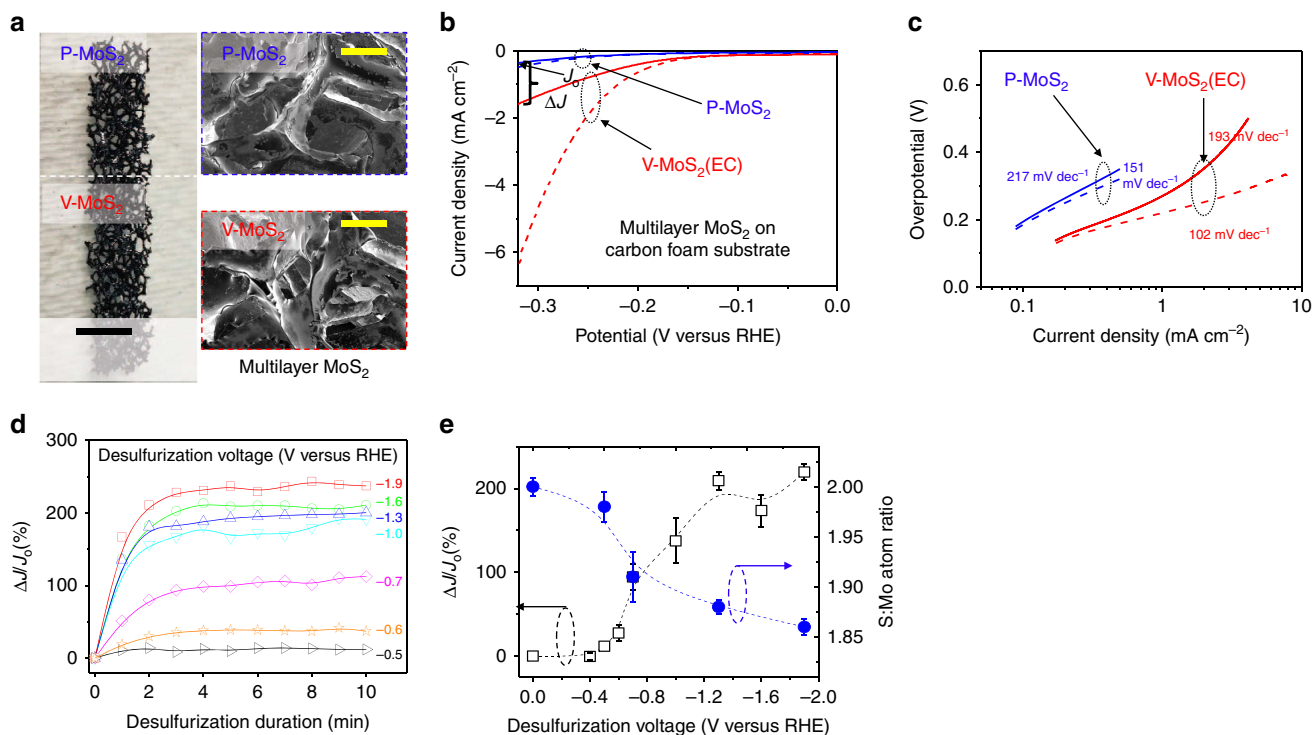


**Figure 4 | HER activity before and after desulfurization of polycrystalline multilayer 2H-MoS<sub>2</sub>.** (a) Optical (left panel; scale bar, 0.5 cm) and SEM images (right panel; scale bar, 0.5 mm) of multilayer MoS<sub>2</sub> film on carbon foam before (P-MoS<sub>2</sub>, upper panel) and after (V-MoS<sub>2</sub>, lower panel) desulfurization at  $-1.3$  V versus RHE for 60 s. (b) LSV of multilayer MoS<sub>2</sub> on carbon foam before and after desulfurization, respectively. All the current densities are defined based on the total electrode surface area. The current density increment is defined as  $\Delta J/J_0$ , where  $J_0$  is the current density at  $-0.32$  V versus RHE before desulfurization. The J-V curves after iR correction are plotted using dashed curves for comparison. (c) The corresponding Tafel plot of the curves in **b**. The calculated Tafel slopes are labelled for each curve. (d) Current density increment versus desulfurization duration at various desulfurization voltages from  $-0.5$  to  $-1.9$  V versus RHE. (e) Current density increment (left, y axis) and S:Mo atom ratio (right, y axis) versus desulfurization voltage at fixed desulfurization duration of 10 min. The error bars represent the s.d.'s.

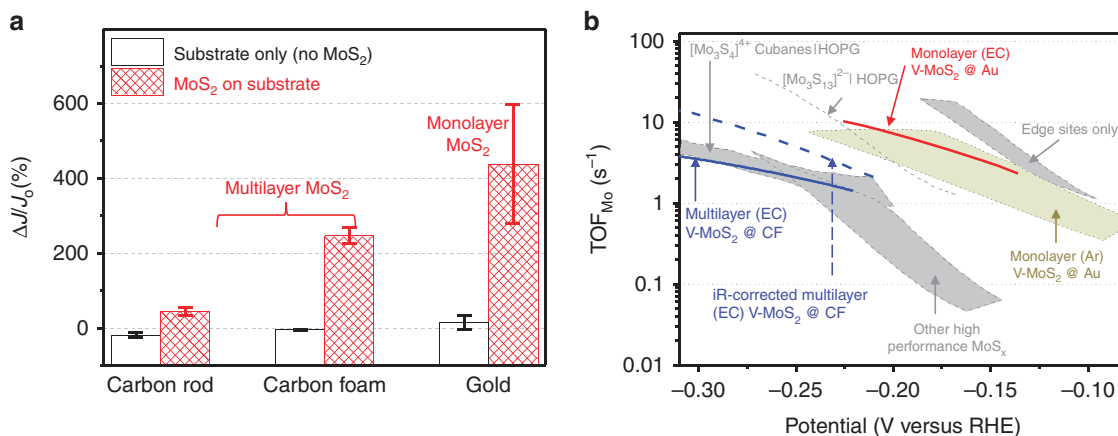


**Figure 5 | Summary of the HER activity of electrochemically desulfurized MoS<sub>2</sub>.** (a) Summary of the desulfurization effect on the enhancement of HER activity for multilayer MoS<sub>2</sub> on carbon rods and carbon foam substrates, and monolayer MoS<sub>2</sub> on Au substrates. The unfilled bars illustrate the effect of electrochemically desulfurization process on the substrates themselves and the effect is negligible. The error bars represent the s.d.'s among the samples. (b) Comparison of turnover frequencies TOF<sub>Mo</sub> per surface Mo atom between our samples and state-of-the-art MoS<sub>x</sub> electrocatalysts. Various state-of-the-art MoS<sub>x</sub> catalysts from ref. 24 are shown with non-bold labels. The light-green-coloured area is for Ar-desulfurized monolayer MoS<sub>2</sub> from ref. 9. The red solid curve is for electrochemically desulfurized monolayer MoS<sub>2</sub> on an Au substrate. The blue solid curve is for electrochemically desulfurized multilayer MoS<sub>2</sub> on carbon foam substrate without iR correction. The blue dashed curve is from electrochemically desulfurized multilayer MoS<sub>2</sub> on a carbon foam substrate with iR correction.

green-coloured area shows the TOF<sub>Mo</sub> range of Ar-desulfurized monolayer MoS<sub>2</sub> (ref. 9). The red and blue solid curves represent the EC desulfurized monolayer MoS<sub>2</sub> on Au substrates and multilayer MoS<sub>2</sub> on carbon foam substrates without iR correction,

respectively. And the blue dashed curve represents the EC desulfurized multilayer MoS<sub>2</sub> on carbon foam with iR correction. One can see that (1) the TOF<sub>Mo</sub> of our desulfurized monolayer MoS<sub>2</sub> (red solid curve) is close to the highest TOF<sub>Mo</sub>; and (2) the

TOF<sub>Mo</sub> values of our desulfurized multilayer MoS<sub>2</sub> catalysts are comparable and slightly higher than most state-of-the-art MoS<sub>x</sub>. They are only lower than edge sites of monolayers (which disregards non-edge sites in the normalization) and amorphous [Mo<sub>3</sub>S<sub>13</sub>]<sup>-2</sup> supported on HOPG (see Supplementary Table 2 and Supplementary Fig. 6 for a quantitative comparison of potential). Our results not only illustrate a general method of EC desulfurization that can be applied to different catalysts, but display high-intrinsic activity in all cases, comparing favourably to the most active sites reported so far. Since our sites are generated from the inert basal plane, our active sites should in principle, work in conjunction with other active sites such as the edge sites.

Although we have focused on HER, the simplest EC reaction, the exact same process can be carried out to generate sulfur vacancies for any other process of interest. MoS<sub>2</sub>-type materials are increasingly being considered for various EC processes such as the electro-catalytic reduction of CO<sub>2</sub> (refs 25,26). There the operating potentials are much closer to the desulfurization potentials, so the possibility of vacancy formation has significant implications. The surface functionalization of MoS<sub>2</sub> in field-effect transistors<sup>27</sup> is another very recent example outside of catalysis where surface vacancies have been exploited. Finally, the formation of surface vacancies simply involves the EC reduction of the chalcogenide on the surface, so similar surface vacancies could in principle be created in other sulfides, selenides, phosphides, oxides and nitrides as well. Our work demonstrates an effective proof of concept for accomplishing this.

## Discussion

In summary, we have theoretically devised and then experimentally validated a facile and scalable method for electrochemically generating catalytically active S-vacancy sites on 2H-MoS<sub>2</sub> under ambient conditions. Once the sulfur atoms are electrochemically reduced, the catalyst is permanently activated. We have demonstrated the generality of this method by applying it to various systems of MoS<sub>2</sub> catalysts, which all show significant improvement in HER activity. The sulfur removal and hence activity increment can be further tuned by varying the applied desulfurization voltage and duration. Although we demonstrate a high per-site TOF, it is worth noting that our samples have limited total activity, which must also be optimized before these catalysts can be considered true viable alternatives to the state-of-the-art. This can be done using the various nanostructuring techniques mentioned earlier, and is the subject of ongoing work. Since the 2H-MoS<sub>2</sub> basal plane constitutes the bulk of industrial MoS<sub>2</sub> catalysts and is present in almost all MoS<sub>2</sub> catalysts, our approach can be used directly to further enhance the HER activity on all of those catalysts.

## Methods

**Theoretical calculations.** All calculations in this work were performed using plane-wave DFT employing periodic boundary conditions as implemented in the Quantum ESPRESSO code. The Bayesian error estimation exchange-correlation functional with van der Waals interactions<sup>28</sup> was used. This functional has been optimized for chemisorption energies as well as van der Waals interactions. The lattice parameters of MoS<sub>2</sub> were determined to be  $a = 3.19$  Å and  $c = 13.05$  Å, in close agreement with experimentally measured values of  $a = 3.162$  Å and  $c = 12.29$  Å (ref. 29). A plane-wave cutoff of 500 eV and a density cutoff of 5,000 eV were used, and a Monkhorst-Pack  $2 \times 2 \times 1$   $k$ -point grid was used to sample the Brillouin zone. Periodic boundary conditions were used in all directions and 11 Å of vacuum was used in the  $z$  direction to separate the slabs, which are 4 Mo atoms  $\times$  4 Mo atoms in size. For the structural relaxation, a convergence criterion of 0.05 eV Å<sup>-1</sup> was used for the maximum force. The reaction free energies,  $\Delta G^0$ , are determined at standard conditions and a potential of  $U = 0$  V as

$$\Delta G^0 = \Delta E + \Delta ZPE - T\Delta S \quad (3)$$

where  $\Delta E$  is the reaction energy,  $\Delta ZPE$  is the difference in zero point energies and  $\Delta S$  is the change in entropy for the reaction step. Additionally, the potential dependence of hydrogen adsorption is including using the computational hydrogen electrode model<sup>14,15</sup>, where

$$\Delta G_{\text{H}^+(\text{aq})} + \Delta G_{\text{e}^-} = \frac{1}{2} \Delta G_{\text{H}(\text{aq})} \quad (4)$$

at a potential of  $U = 0$  V versus RHE. The effect of an applied potential can then be included by shifting the free energy using  $\Delta G = \Delta G^0 + eU$ . The results in the free energy diagram shown in Fig. 2 were determined using this approach. Although reaction barriers were not calculated, they are known to scale with reaction energies<sup>30</sup>, so our results should still be sufficient for illustrating the relevant trends. Further information about the computational set-up is described in Supplementary Note 1.

**Fabrication of continuous 2H-MoS<sub>2</sub> monolayers on Au electrode.** A customized tube furnace system was employed to grow continuous 2H-MoS<sub>2</sub> monolayers. As-purchased molybdenum trioxide (MoO<sub>3</sub>) and sulfur (S) powder were loaded in alumina boats separately. The alumina boat containing MoO<sub>3</sub> was placed in the centre of the tube furnace where the temperature was set at 750 °C during the growth, and the alumina boat containing S was placed upstream where the temperature was about 200 °C during the growth. Argon gas was used as the carrier gas to bring S vapour to the centre of the tube furnace at atmospheric pressure. A SiO<sub>2</sub>/Si wafer suspended on the alumina boat was used as the growth substrate for the MoS<sub>2</sub> monolayers. The as-grown MoS<sub>2</sub> monolayers are almost continuous in an area larger than 3 mm in diameter (the size of our EC compression cell) for the EC measurements. A continuous MoS<sub>2</sub> monolayer with high coverage and large flake size was selected and transferred onto Au (80 nm)/titanium (10 nm)-coated SiO<sub>2</sub>/Si wafer, and cleaned thoroughly in hot acetone (56 °C for 10 min) and chloroform (60 °C for 1 h) sequentially. As both solvents vaporize quickly when heated up, the beaker was partially covered to reduce the loss of solvent.

**Fabrication of polycrystalline 2H-MoS<sub>2</sub> on carbon electrodes.** Polycrystalline multilayer 2H-MoS<sub>2</sub> was grown on commercial carbon rods and carbon foams through thermolysis of ammonium thiomolybdates [(NH<sub>4</sub>)<sub>2</sub>MoS<sub>4</sub>]. Commercial (NH<sub>4</sub>)<sub>2</sub>MoS<sub>4</sub> was dissolved in dimethylformamide using a concentration of 1.25 wt%. The solution was stirred and sonicated to completely dissolve (NH<sub>4</sub>)<sub>2</sub>MoS<sub>4</sub> particles. Then, the cleaned carbon rod and foam were dipped in the solution, and then dried in air at 50 °C. The carbon electrodes with coated (NH<sub>4</sub>)<sub>2</sub>MoS<sub>4</sub> were heated in a tube furnace in the presence of S vapour with argon as the carrier gas at 400 °C and 1 atm for 1 h. During the heating process, (NH<sub>4</sub>)<sub>2</sub>MoS<sub>4</sub> decomposed and formed polycrystalline MoS<sub>2</sub> (see Supplementary Fig. 3 and Supplementary Note 4 for Raman spectra<sup>31</sup>). The control samples that contain the carbon substrates only (Fig. 4d) were fabricated using the same sulfurization process.

**XPS measurements.** XPS characterizations were conducted in UHV ( $5 \times 10^{-10}$  Torr) with excitation by Al (ka) radiation. The S:Mo atom ratios were estimated from the XPS peak area ratio of S 2p to that of Mo 3d states. The XPS peak area ratio of S 2p to Mo 3d states for as-grown pristine MoS<sub>2</sub> was set as 2.0 to normalize other samples.

**ICP-OES measurements.** ICP-OES was carried out using a Thermo scientific ICAP 6300 Duo View Spectrometer. A commercial high-quality standard solution of Mo and S elements with 10 ppm concentration in 2% nitric acid was used. As a blank solution 2.8% nitric acid was used and mixed with the standard solution to make 2.4% nitric acid of the quality control standard solution. MoS<sub>2</sub> samples were dissolved in 69% concentrated nitric acid solvent for 18 h. Then the impurity particles of the sample solution were removed by centrifugation at a speed of 4,000 rpm for 15 min. Finally, a clear solution was taken and diluted to 8% nitric acid solution and injected into ICP-OES to get the elemental ratio of Mo and S.

**EC measurements.** A Gamry 1000 potentiostat was employed for the EC measurements in this work. A three-electrode EC cell was used with 0.5 M sulfuric acid (H<sub>2</sub>SO<sub>4</sub>) as the electrolyte (the desulfurization process was performed in the same electrolyte). The working electrode was MoS<sub>2</sub>, and the counter electrode was a Pt wire. The reference electrode was a commercial Ag|AgCl electrode. The desulfurization of monolayer MoS<sub>2</sub> samples (Fig. 3) was performed using LSV with a sweeping speed of 50 mV s<sup>-1</sup>. The desulfurization for the multilayer MoS<sub>2</sub> samples (Fig. 4) was performed using chronoamperometry with a 60 s time interval unless specified otherwise. The stability of desulfurized polycrystalline multilayer MoS<sub>2</sub> was tested at constant potential of  $-0.32$  V versus RHE (Supplementary Fig. 4 and Supplementary Note 5).

**Data availability.** The data that support the findings of this study are available from the corresponding author on reasonable request.

## References

- Hinnemann, B. *et al.* Biomimetic hydrogen evolution: MoS<sub>2</sub> nanoparticles as catalyst for hydrogen evolution. *J. Am. Chem. Soc.* **127**, 5308–5309 (2005).
- Jaramillo, T. F. *et al.* Identification of active edge sites for electrochemical H<sub>2</sub> evolution from MoS<sub>2</sub> nanocatalysts. *Science* **317**, 100–102 (2007).
- Kibsgaard, J., Chen, Z., Reinecke, B. N. & Jaramillo, T. F. Engineering the surface structure of MoS<sub>2</sub> to preferentially expose active edge sites for electrocatalysis. *Nat. Mater.* **11**, 963–969 (2012).
- Kong, D. *et al.* Synthesis of MoS<sub>2</sub> and MoSe<sub>2</sub> films with vertically aligned layers. *Nano Lett.* **13**, 1341–1347 (2013).
- Li, D. J. *et al.* Molybdenum sulfide/N-doped CNT forest hybrid catalysts for high-performance hydrogen evolution reaction. *Nano Lett.* **14**, 1228–1233 (2014).
- Voiry, D., Salehi, M., Silva, R., Fujita, T. & Chen, M. Conducting MoS<sub>2</sub> nanosheets as catalysts for hydrogen evolution reaction. *Nano Lett.* **13**, 6222–6227 (2013).
- Lukowski, M. A. *et al.* Enhanced hydrogen evolution catalysis from chemically exfoliated metallic MoS<sub>2</sub> nanosheets. *J. Am. Chem. Soc.* **135**, 10274–10277 (2013).
- Wang, H. *et al.* Electrochemical tuning of vertically aligned MoS<sub>2</sub> nanofilms and its application in improving hydrogen evolution reaction. *Proc. Natl Acad. Sci. USA* **110**, 19701–19706 (2013).
- Li, H. *et al.* Activating and optimizing MoS<sub>2</sub> basal planes for hydrogen evolution through the formation of strained sulfur vacancies. *Nat. Mater.* **15**, 48–53 (2015).
- Ye, G. *et al.* Defects engineered monolayer MoS<sub>2</sub> for improved hydrogen evolution reaction. *Nano Lett.* **16**, 1097–1103 (2016).
- Ma, Q. *et al.* Controlled argon beam-induced desulfurization of monolayer molybdenum disulfide. *J. Phys.* **25**, 252201 (2013).
- Lee, H. Y., Cho, W. S., Oh, S. M., Wiemhöfer, H. D. & Göpel, W. Active reaction sites for oxygen reduction in La<sub>0.9</sub>Sr<sub>0.1</sub>MnO<sub>3</sub>/YSZ electrodes. *J. Electrochem. Soc.* **142**, 2659–2664 (1995).
- Tsai, C., Abild-Pedersen, F. & Nørskov, J. K. Tuning the MoS<sub>2</sub> edge-site activity for hydrogen evolution via support interactions. *Nano Lett.* **14**, 1381–1387 (2014).
- Nørskov, J. K. *et al.* Origin of the overpotential for oxygen reduction at a fuel-cell cathode. *J. Phys. Chem. B* **108**, 17886–17892 (2004).
- Peterson, A. A., Abild-Pedersen, F., Studt, F., Rossmeisl, J. & Nørskov, J. K. How copper catalyzes the electroreduction of carbon dioxide into hydrocarbon fuels. *Energy Environ. Sci.* **3**, 1311 (2010).
- Shi, C., O'Grady, C. P., Peterson, A. A., Hansen, H. A. & Nørskov, J. K. Modeling CO<sub>2</sub> reduction on Pt(111). *Phys. Chem. Chem. Phys.* **15**, 7114 (2013).
- Tsai, C., Chan, K., Abild-Pedersen, F. & Nørskov, J. K. Active edge sites in MoSe<sub>2</sub> and WSe<sub>2</sub> catalysts for the hydrogen evolution reaction: a density functional study. *Phys. Chem. Chem. Phys.* **16**, 13156–13164 (2014).
- Tsai, C., Chan, K., Nørskov, J. K. & Abild-Pedersen, F. Theoretical insights into the hydrogen evolution activity of layered transition metal dichalcogenides. *Surf. Sci.* **640**, 133–140 (2015).
- Voiry, D. *et al.* The role of electronic coupling between substrate and 2D MoS<sub>2</sub> nanosheets in electrocatalytic production of hydrogen. *Nat. Mater.* **15**, 1003–1009 (2016).
- Liu, K.-K. *et al.* Growth of large-area and highly crystalline MoS<sub>2</sub> thin layers on insulating substrates. *Nano Lett.* **12**, 1538–1544 (2012).
- Li, H. *et al.* Kinetic study of hydrogen evolution reaction over strained MoS<sub>2</sub> with sulfur-vacancies using scanning electrochemical microscopy. *J. Am. Chem. Soc.* **138**, 5123–5129 (2016).
- Yu, Y. *et al.* Layer-dependent electrocatalysis of MoS<sub>2</sub> for hydrogen evolution. *Nano Lett.* **14**, 553–558 (2014).
- Li, Y. *et al.* MoS<sub>2</sub> nanoparticles grown on graphene: an advanced catalyst for the hydrogen evolution reaction. *J. Am. Chem. Soc.* **133**, 7296–7299 (2011).
- Benck, J. D., Hellstern, T. R., Kibsgaard, J., Chakhranont, P. & Jaramillo, T. F. Catalyzing the hydrogen evolution reaction (HER) with molybdenum sulfide nanomaterials. *ACS Catal.* **4**, 3957–3971 (2014).
- Chan, K., Tsai, C., Hansen, H. A. & Nørskov, J. K. Molybdenum sulfide and selenides as possible electrocatalysts for CO<sub>2</sub> reduction. *ChemCatChem.* **6**, 1899–1905 (2014).
- Asadi, M. *et al.* Robust carbon dioxide reduction on molybdenum disulfide edges. *Nat. Commun.* **5**, 4470 (2014).
- Sim, D. M. *et al.* Controlled doping of vacancy-containing few-layer MoS<sub>2</sub> via highly stable thiol-based molecular chemisorption. *ACS Nano* **9**, 12115–12123 (2015).
- Wellendorff, J. *et al.* Density functionals for surface science: exchange-correlation model development with Bayesian error estimation. *Phys. Rev. B* **85**, 235149 (2012).
- Jellinek, F., Brauer, G. & Müller, H. Molybdenum and niobium sulfides. *Nature* **185**, 376–377 (1960).
- Bligard, T. *et al.* The Brønsted–Evans–Polanyi relation and the volcano curve in heterogeneous catalysis. *J. Catal.* **224**, 206–217 (2004).
- Li, H. *et al.* From bulk to monolayer MoS<sub>2</sub>: evolution of Raman scattering. *Adv. Funct. Mater.* **22**, 1385–1390 (2012).

## Acknowledgements

F.A.-P. and J.K.N. acknowledge financial support from the U.S. Department of Energy (DOE), Office of Basic Energy Sciences from the SUNCAT Centre for Interface Science and Catalysis. C.T. acknowledges support from the National Science Foundation Graduate Research Fellowship Program (GRFP) Grant DGE-114747. H.L. and X.Z. acknowledge the financial support from the 2013 Global Research Outreach (GRO) Program (Award #: IC2012-1318) of the Samsung Advanced Institute of Technology (SAIT) and Samsung R&D Centre America, Silicon Valley (SRA-SV). H.L. acknowledges support from the NAP fellowship of Nanyang Technological University Singapore. We thank Dr Karen Chan for fruitful discussions regarding the calculations.

## Author contributions

C.T., H.L., S.P., J.K.N., X.Z. and F.A.-P. conceived the idea and designed the experiments. H.L. and S.P. performed the material growth, electrode fabrication and EC measurements. C.T. carried out the calculations. J.P. conducted the TEM measurements. H.S.H. conducted EIS measurements. C.T., J.K.N. and F.A.-P. analysed the theoretical results. C.T., H.L., S.P., X.Z. and F.A.-P. wrote the manuscript, and all authors discussed the results and commented on the manuscript.

## Additional information

**Supplementary Information** accompanies this paper at <http://www.nature.com/naturecommunications>

**Competing interests:** The authors declare no competing financial interests.

**Reprints and permission** information is available online at <http://npg.nature.com/reprintsandpermissions/>

**How to cite this article:** Tsai, C. *et al.* Electrochemical generation of sulfur vacancies in the basal plane of MoS<sub>2</sub> for hydrogen evolution. *Nat. Commun.* **8**, 15113 doi: 10.1038/ncomms15113 (2017).

**Publisher's note:** Springer Nature remains neutral with regard to jurisdictional claims in published maps and institutional affiliations.



This work is licensed under a Creative Commons Attribution 4.0 International License. The images or other third party material in this article are included in the article's Creative Commons license, unless indicated otherwise in the credit line; if the material is not included under the Creative Commons license, users will need to obtain permission from the license holder to reproduce the material. To view a copy of this license, visit <http://creativecommons.org/licenses/by/4.0/>

© The Author(s) 2017